Epigenetic MRI: Noninvasive imaging of DNA methylation in the brain

Fan Lam[a,b,c,d,e,1], James Chu[b,d,1], Ji Sun Choi[b,d], Chang Cao[b,c], T. Kevin Hitchens[f], Scott K. Silverman[g], Zhi-Pei Liang[a,b,e,h], Ryan N. Dilger[b,c,i,j], Gene E. Robinson[c,d,j,k,2], and King C. Li[b,d,e,2]

[a]Department of Bioengineering, University of Illinois Urbana–Champaign, Urbana, IL 61801; [b]Beckman Institute for Advanced Science and Technology, University of Illinois Urbana–Champaign, Urbana, IL 61801; [c]Carl R. Woese Institute for Genomic Biology, University of Illinois Urbana–Champaign, Urbana, IL 61801; [d]Carle-Illinois College of Medicine, University of Illinois Urbana–Champaign, Urbana, IL 61801; [e]Cancer Center at Illinois, University of Illinois Urbana–Champaign, Urbana, IL 61801; [f]Department of Neurobiology and Animal Imaging Center, University of Pittsburgh, Pittsburgh, PA 15203; [g]Department of Chemistry, University of Illinois Urbana–Champaign, Urbana, IL 61801; [h]Department of Electrical and Computer Engineering, University of Illinois Urbana–Champaign, Urbana, IL 61801; [i]Department of Animal Sciences, University of Illinois Urbana–Champaign, Urbana, IL 61801; [j]Neuroscience Program, University of Illinois Urbana–Champaign, Urbana, IL 61801; and [k]Department of Entomology, University of Illinois Urbana–Champaign, Urbana, IL 61801

Contributed by Gene E. Robinson; received November 5, 2021; accepted January 21, 2022; reviewed by Daniel Geschwind and Chien Ho

Both neuronal and genetic mechanisms regulate brain function. While there are excellent methods to study neuronal activity in vivo, there are no nondestructive methods to measure global gene expression in living brains. Here, we present a method, epigenetic MRI (eMRI), that overcomes this limitation via direct imaging of DNA methylation, a major gene-expression regulator. eMRI exploits the methionine metabolic pathways for DNA methylation to label genomic DNA through ^{13}C-enriched diets. A ^{13}C magnetic resonance spectroscopic imaging method then maps the spatial distribution of labeled DNA. We validated eMRI using pigs, whose brains have stronger similarity to humans in volume and anatomy than rodents, and confirmed efficient ^{13}C-labeling of brain DNA. We also discovered strong regional differences in global DNA methylation. Just as functional MRI measurements of regional neuronal activity have had a transformational effect on neuroscience, we expect that the eMRI signal, both as a measure of regional epigenetic activity and as a possible surrogate for regional gene expression, will enable many new investigations of human brain function, behavior, and disease.

gene expression | DNA methylation | isotope labeling | NMR spectroscopy | spectroscopic imaging

The brain is ever-changing in structure and function as a result of development, aging, environmental influence, and disease. Two fundamental mechanisms underpin these changes: neuronal activation, which occurs over relatively short time scales (milliseconds, seconds, and minutes), and gene expression, which occurs over longer time scales (hours, days, or even longer) (1–3). Advances in imaging technology have transformed how we investigate these mechanisms.

Functional MRI (fMRI) has revolutionized our understanding of the human brain by providing a powerful nondestructive method to image neural activity (4–7). In contrast, the technologies to image gene expression have been limited to methods that require invasive sampling and tissue processing (8–11). Although these techniques have provided tremendous knowledge about gene expression and gene regulation in the brain, especially in animal models, their destructive nature makes longitudinal studies of the same samples impossible, thus limiting our ability to translate and expand scientific discoveries to human brains. This is especially unfortunate because longer-term changes in brain function play critical roles in both brain diseases and responses of the brain to environmental change (1–3). The ability to measure and visualize gene expression and regulation in the brain noninvasively would revolutionize the study of brain function, behavior, and disease (12).

Efforts to map brain gene expression and regulation in living organisms to date have involved imaging reporter genes or associated enzymes using optical techniques, positron emission tomography (PET), or MRI (13–17). These methods are either limited to model organisms or require transgenic animals engineered to express a particular reporter gene and an exogenous contrast probe interacting with the reporter gene to produce the desired images (15, 16). Therefore, such methods have no clear path for translation to humans. Furthermore, these methods are limited to just a few genes and, therefore, cannot provide a comprehensive portrait of gene expression.

PET imaging of histone deacetylases (HDACs) in the human brain was recently demonstrated, using a radioactive tracer that can pass the blood–brain barrier (BBB) and target HDAC isoforms (18, 19). This probes a major form of epigenetic gene regulation, histone acetylation, but PET requires introducing radioactive materials into the body, and it only targets one of the enzymes that regulates histone acetylation, rather than histone acetylation itself. Moreover, PET lacks the specificity to distinguish between the target molecule and downstream metabolic products (20–22). Other imaging epigenetics approaches have studied correlations between brain MRI and gene expression or methylation in postmortem tissues, saliva, or blood

Significance

Dynamic epigenetic activity is a fundamental mechanism underpinning how the brain changes its function during development and aging and in response to environmental and disease stimuli. We developed a technology called epigenetic MRI (eMRI) that enables noninvasive imaging of DNA methylation in the brain, a major epigenetic mechanism. eMRI reveals strong regional differences in global DNA methylation in pig brains, a model with stronger resemblance to human brains than are rodents. Given the noninvasive nature of eMRI, our results pave the way for a DNA-methylation imaging paradigm for living human brains. We expect eMRI to enable many studies to unravel the molecular control of brain function and disease.

Author contributions: F.L., S.K.S., Z.-P.L., G.E.R., and K.C.L. designed research; F.L., J.C., J.S.C., C.C., T.K.H., S.K.S., Z.-P. L, R.N.D., G.E.R. and K.C.L. performed research; F.L., J.C., J.S.C., C.C., T.K.H., S.K.S., Z.-P.L., R.N.D., and K.C.L. analyzed data; F.L., J.C., J.S.C., C.C., T.K.H., S.K.S., Z.-P.L., R.N.D., G.E.R., and K.C.L. wrote the paper; and F.L., J.C., J.S.C., C.C., S.K.S., Z.-P.L., R.N.D., and K.C.L. provided technical implementation.

Reviewers: D.G., University of California Los Angeles Center for Autism Research and Treatment; and C.H., Carnegie Mellon University.

Competing interest statement: Provisional patent filed through the University of Illinois Urbana–Champaign.

[1]F.L. and J.C. contributed equally to this work.

[2]To whom correspondence may be addressed. Email: generobi@illinois.edu or kingli@illinois.edu.

This article contains supporting information online at http://www.pnas.org/lookup/suppl/doi:10.1073/pnas.2119891119/-/DCSupplemental.

Published March 2, 2022.

(23–28); although useful, they can only provide indirect insights into the brain gene expression and regulation.

We present successful direct imaging of brain DNA methylation using an approach we call epigenetic MRI (eMRI), which integrates stable isotope 5-methyl-2′-deoxycytidine (5mdC) labeling through diet and magnetic resonance spectroscopic imaging (MRSI). Using pigs fed by a customized diet enriched in ^{13}C-methionine (^{13}C-Met) and innovations to ^{13}C-MRSI, we report robust mapping in intact brain hemispheres that revealed strong regional differences in DNA methylation. We chose pigs as a surrogate to assess feasibility of translation to humans because of stronger similarities in brain size and anatomy than rodent models (29). Significant eMRI signal differences were observed in animals fed with enriched diet for different numbers of days, demonstrating the dynamic nature of this signal. Given the noninvasiveness of our method, these results provide a path toward a global DNA-methylation brain-imaging paradigm for humans. Because DNA methylation is one of the major regulators of gene expression, eMRI promises to become a powerful tool to understand the molecular basis of brain function and disease.

Results

In Vivo Brain DNA-Methylation Labeling Using ^{13}C-Met–Enriched Diet. A key feature of eMRI is the use of a natural amino acid involved in DNA methylation that is labeled with an NMR-active stable isotope, making methylated DNA detectable with noninvasive imaging (Fig. 1). We chose ^{13}C-Met because Met is an essential amino acid and the major methyl group donor for DNA methylation. Met is also commonly used as a nutritional supplement and approved for human use. To validate our labeling approach, we designed a special diet that replaced all protein with free amino acids in the proper proportions and substituted all Met with enriched ^{13}C-Met. We fed this diet to piglets starting from postnatal day (PND) 1 (Fig. 1*A*). The ingested ^{13}C-Met crosses the BBB (30–32) and is converted into ^{13}C-*S*-adenosylmethionine (^{13}C-SAM), which then provides the ^{13}C-methyl group for cytosine methylation, effectively labeling the 5mdC in brain genomic DNA (Fig. 1*B*). This is similar to the labeling scheme used to study the conversion of 5mdC to 5-hydroxymethyl-2′-deoxycytidine in laboratory mice with triply deuterated ^{13}C-Met (33). After diet replacement for 10 or 32 d, animals were euthanized. Following brain dissection, one hemisphere was used for tissue sampling from various brain regions, DNA extraction, and analysis by liquid chromatography–tandem mass spectrometry (LC-MS/MS) to confirm DNA labeling; the other intact hemisphere was used for noninvasive eMRI (Fig. 1*C*). Control animals were fed with the same formula for 10 or 32 d, but all ^{13}C-Met was replaced with non-isotope-labeled Met.

LC-MS/MS analysis revealed effective labeling of brain 5mdC after feeding for 10 d with the ^{13}C-Met–enriched diet. Relative to controls, we detected a 3 to 4% increase in ^{13}C-labeled 5mdC (as a fraction of total 5mdC) across eight different sampled brain regions (Fig. 2*A*). Feeding for 32 d resulted in much stronger labeling, with >12% increase in ^{13}C-5mdC compared to the age-matched controls (Fig. 2*B*). The baseline ^{13}C-labeled 5mdC signal was ∼5% in the controls at both ages (Fig. 2*C*), which is consistent with the 1.1% natural abundance of the ^{13}C isotope and accounting for the five carbons in 5mdC (34).

The 32-d-labeled samples produced >2× labeling percentage compared to the 10-d-labeled samples (Fig. 2*D*; $P < 0.001$, one-way ANOVA). As expected, the baseline ^{13}C-5mdC percentage did not differ among the eight brain regions or between the control animals fed for either 10 or 32 d (Fig. 2 *C* and *E*). Differences in ^{13}C-5mdC percentage across brain regions in the labeled samples were not statistically significant for either time point (Fig. 2*E*). Representative LC-MS/MS data revealing the ^{13}C-5mdC and 5mdC peaks are in *SI Appendix*, Fig. S1.

From these data, two interesting observations were made about DNA-methylation dynamics in the brain. First, there was a nonlinear increase in labeling from day 10 to 32, much greater than from day 0 to 10 (Fig. 2*D*). This increase occurred despite a relative decrease in daily ^{13}C-Met intake (in terms of milligrams per kilogram of body weight per day) due to rapid increases in body weight over the same time period. We speculate this to be the result of an increase in DNA-methylation events and the methylation–demethylation turnover cycle as part of normal brain development. Second, the approximately twofold increase in labeling percentage detected in animals fed ^{13}C-Met for 32 d relative to 10 d vastly outpaced the ∼20% increase in brain volume that occurred during the same period (Fig. 2*F*). This finding suggests that increases in tissue volume and neuronal density during brain development are not the only drivers of increased ^{13}C-methyl incorporation into brain DNA. This implicates either intrinsic age-related changes in methylation dynamics or extrinsic processes, such as learning and memory formation, which are known to affect brain DNA methylation (1–3, 35–37). They may cause unlabeled methyl groups to be replaced with ^{13}C-labeled methyl groups through

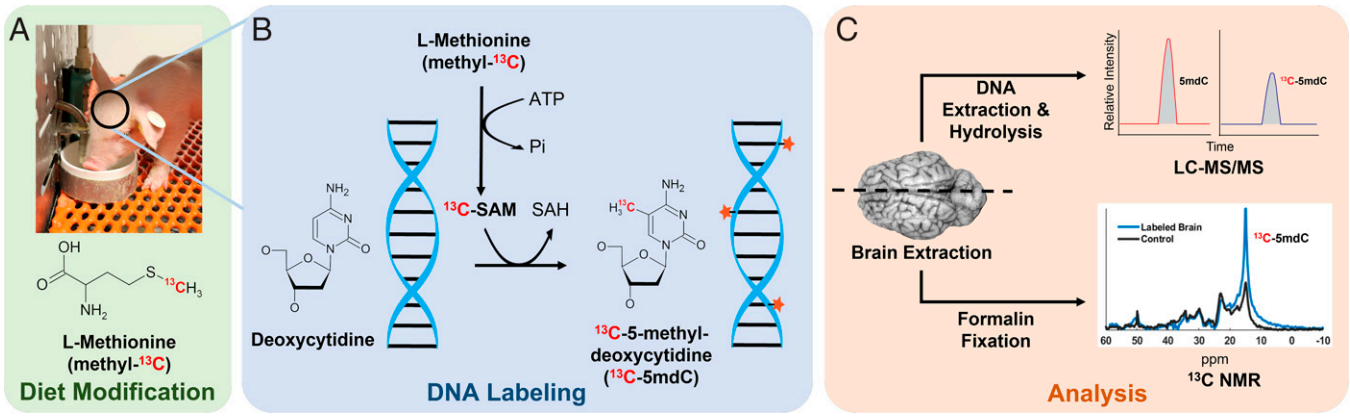

Fig. 1. Design of dietary ^{13}C labeling of genomic DNA in the brain and eMRI. (*A*) A special diet enriched with ^{13}C-Met was ingested by neonatal piglets through a milk-replacement formula for either 10 or 32 d. Diet for age-matched controls had all ^{13}C-Met replaced by regular Met. (*B*) Ingested ^{13}C-Met passes through the BBB and is converted to ^{13}C-SAM, which methylates the DNA, producing ^{13}C-methyl-labeled DNA. (*C*) Brain tissues were sampled from one hemisphere for DNA extraction and LC-MS/MS analysis to validate labeling. The other intact hemisphere was analyzed using nondestructive ^{13}C-NMR and -MRSI, another key feature of eMRI.

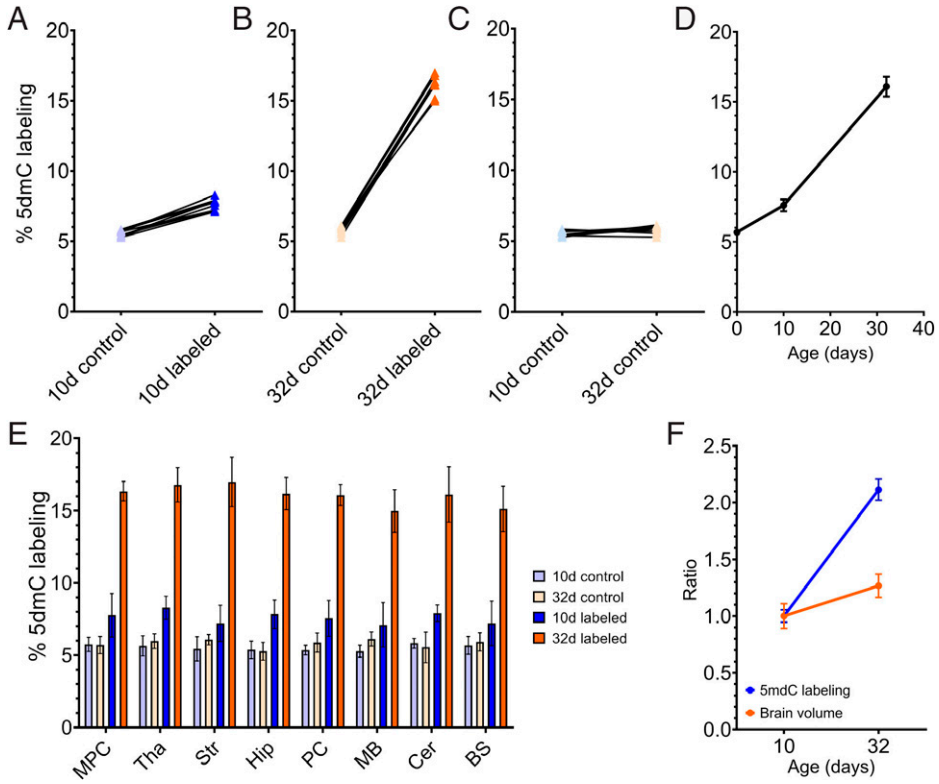

Fig. 2. Dietary ^{13}C labeling of brain genomic DNA confirmed by LC-MS/MS. (*A*) After 10 d of the ^{13}C-Met–enriched diet, ^{13}C-5mdC in the brain DNA (ratio of ^{13}C-5mdC to total 5mdC) increased from ~5% to 8-9%. (*B*) After 32 d, ^{13}C-5mdC in the brain DNA significantly increased to ~15-18%. (*C*) Age-matched controls for both 10 d and 32 d diets had ~5% ^{13}C-5mdC, consistent with the 1.1% natural abundance of the ^{13}C isotope. (*D*) Because ~5% ^{13}C-5mdC can be assumed at birth, we back-extrapolated the curve for percentage vs. days of diet. A nonlinear increase in labeling was observed, with the increase from day 10 to 32 much greater than for day 0 to 10. (*E*) A more detailed comparison of labeling percentages for different diet groups and brain regions; error bars indicate SDs. No regional differences were observed for the controls. (*F*) The ^{13}C-5mdC increase from 10-32 d with ^{13}C diet (~2×) is considerably larger than the brain volume increase that occurred over the same time period (~20%). All measurements are within the linear range of our LC-MS/MS protocol. Brain regions: medial prefrontal cortex (MPC), thalamus (Tha), striatum (Str), hippocampus (Hip), perirhinal cortex (PC), midbrain (MB), cerebellum (Cer), and brainstem (BS).

turnover or cause unmethylated cytosine to be methylated. These results also demonstrate the responsiveness of the eMRI signal to changing experimental conditions.

Noninvasive Detection of Labeled Methylated DNA Using ^{13}C-NMR. Strong isotope labeling of methylated DNA in the brain enables the possibility of using noninvasive isotopic detection methods. For eMRI, we chose ^{13}C-NMR to detect and quantify the ^{13}C-labeled 5mdC in genomic DNA. The ^{13}C-NMR and imaging using isotope-enriched molecules have been used in various basic biological studies and clinical applications (38–41). It offers several unique advantages: 1) Its nondestructive and nonradioactive nature allows for in vivo translation to humans; 2) its broad chemical-shift dispersion allows for detecting signals specifically from ^{13}C-5mdC in genomic DNA relative to ^{13}C signals from other molecules; and 3) ^{13}C has low natural abundance (~1.1%), which can increase specific signal detection from the ^{13}C-enriched diet.

We first performed a proof-of-principle in vitro experiment using synthetic DNA oligonucleotides with a well-defined number of 5mdC in the sequence. Two results from the ^{13}C-NMR data obtained from these oligonucleotides demonstrated the feasibility of this approach (*SI Appendix*, Fig. S2). First, we specifically detected the ^{13}C signal from the methyl groups on 5mdC in the DNA. Second, we identified the chemical shift of interest for the ^{13}C-5mdC (~15 ppm) for the subsequent brain experiments.

One important challenge for in vivo ^{13}C-NMR is sensitivity. Even at 100% enrichment, the sensitivity of ^{13}C detection is still much lower than ^{1}H, which is commonly imaged in vivo. We overcame this challenge by integrating effective labeling using enriched ^{13}C-Met, ultrahigh-field imaging systems, and advanced signal-processing techniques. We imaged the ^{13}C-labeled brains using a 11.7-Tesla (T) microimaging system (Fig. 3) and obtained whole-sample ^{13}C-NMR spectra from eight brains (two labeled for 10 d, two labeled for 32 d, and two control unlabeled brains at both 10 and 32 d; Fig. 3 *C–E*). A significant signal difference attributed to ^{13}C-5mdC at ~15 ppm (as expected based on the data from the synthetic oligonucleotides) was observed between the control and labeled brains, and the 32-d-labeled brain exhibited significantly stronger signal than the 10-d-labeled and control brains (Fig. 3*F*). The whole-sample spectra were parametrically fitted using an in-house method to quantify the ^{13}C-NMR 5mdC signal (*SI Appendix*, Fig. S3). The signal increase from 10-d to 32-d labeling matched well with the increase in labeling percentage measured by LC-MS/MS analysis at the whole-brain level (but not at the regional level, as shown below) and again significantly outpaced brain volume growth (Fig. 3*G*). These results confirm that increased labeling and the resulting eMRI signals are not driven solely by increases in brain volume and cell density and may be dynamically responsive to neurodevelopmental changes.

Regional Differences in Brain DNA Methylation Revealed by eMRI. The ability of ^{13}C-NMR spectroscopy to noninvasively detect ^{13}C-5mdC signals from genomic DNA establishes the premise of using ^{13}C-MRSI to image brain DNA methylation in vivo by

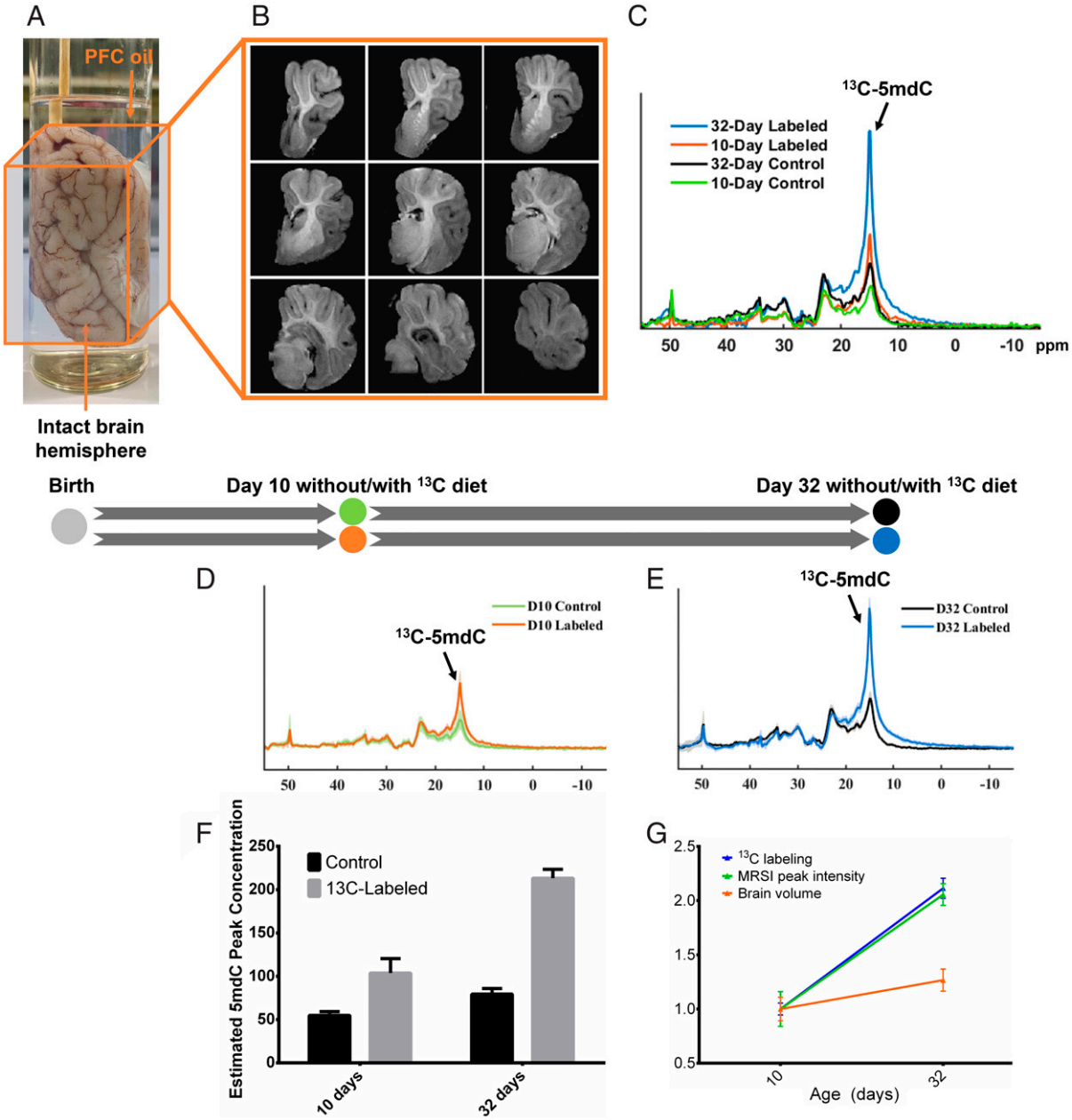

Fig. 3. The ^{13}C-NMR detects labeled DNA and age-dependent labeling in the brain. (*A*) Sample setup for spectroscopy and imaging experiments. The intact brain hemisphere was submerged in PFC (perfluorocarbon) oil for susceptibility matching to improve magnetic field homogeneity. (*B*) A 3D MR image from one of the brain samples. (*C*) Whole-sample ^{13}C-NMR spectra acquired from different brains at different time points and dietary conditions, i.e., 10 d control diet (green), 10 d ^{13}C-Met diet (orange), 32 d control diet (black), and 32 d ^{13}C-Met diet (blue). Data for each sample were acquired in 9-h experiments. (*D* and *E*) Eight brain hemispheres were measured, four for each time point and two for each dietary condition among the four (without and with ^{13}C-Met diet). Consistent results were obtained from each group. Labeled samples, D10 (10 d) in *D* or D32 (32 d) in *E*, produced significantly stronger ^{13}C-5mdC signals (at ~15 ppm; black arrows) compared to age-matched controls. (*F*) Brains labeled for 32 d exhibited significantly stronger signals than those labeled for 10 d (y-axis is in an institutional unit). The signal increase for the controls from 10 to 32 d was due to brain growth and is attributed to natural abundance ^{13}C-NMR signals from 5mdC and methyl groups on thymidine, with the latter a larger contributor due to higher abundance. Nevertheless, the 10-d-labeled sample still showed a stronger signal than the 32 d control, indicating that the signals measured are primarily from ^{13}C-5mdC labeling. (*G*) The signal increase from 10 d to 32 d labeled brains approximately matches the labeling percentage increment measured by LC-MS/MS (Fig. 2*F*) and substantially outpaced brain volume growth.

mapping ^{13}C-labeled 5mdC, another key feature of eMRI. We tested this possibility by performing ^{13}C-MRSI with a subspace imaging strategy (*Materials and Methods*) on brain samples to image DNA methylation.

Our ^{13}C-MRSI method robustly mapped the spatial distribution of ^{13}C-5mdC in brain. The 32 d labeled brains produced clearly discernible regional variation in ^{13}C-5mdC levels (Fig. 4 *A* and *B* and *SI Appendix*, Fig. S4). The localized ^{13}C-NMR spectra extracted from several representative anatomical brain regions confirmed the regional signal variations attributed to the ^{13}C-5mdC peak at ~15 ppm (Fig. 4*C*). The putamen, caudate, and thalamus regions showed the strongest signals, while the temporal and occipital lobes were among the regions showing weaker signals (Fig. 4 *C* and *D*). These regional measurements were confirmed to yield strong and statistically significant differences using pairwise Kruskal–Wallis with Dunn's

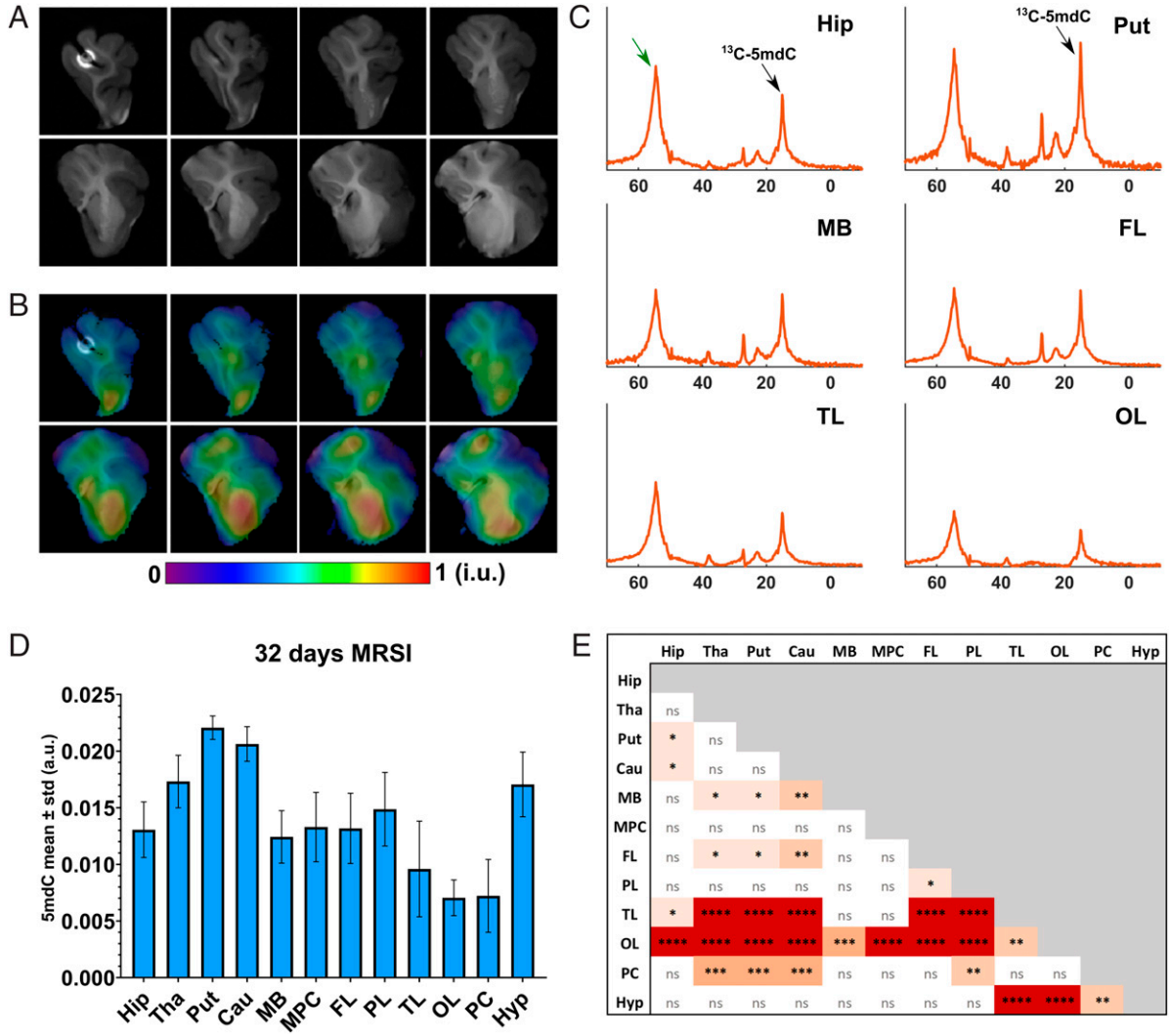

Fig. 4. Mapping regional variation of ^{13}C-labeled DNA in the brain. (*A*) Anatomical MR images corresponding to different slices across the intact 3D imaging volume. (*B*) Spatial maps of labeled DNA methylation overlaid on the same images in *A*. The maps were normalized with a maximum intensity of one (arbitrary institutional units [i.u.]). Clear spatial variation of labeled DNA methylation is observed. (*C*) Localized ^{13}C-NMR spectra from different brain regions (averaged for the voxels within the same region) also exhibited clear regional variation for the peak assigned to ^{13}C-5mdC. The peak at ~55 ppm indicated by the green arrow is hypothesized to be related to lipid metabolism (*SI Appendix*, Fig. S3). (*D*) Quantitative comparison of ^{13}C-5mdC signal differences across brain regions (error bars indicate the SDs for individual regions). Cerebellum and parts of brainstem were not included because they did not fit into the RF probes used in the imaging system. (*E*) Pairwise Kruskal–Wallis with Dunn's multiple comparison tests reveal that several regions produced significantly different ^{13}C-5mdC signals and thus different amounts of labeled methylated DNA. $*P < 0.05$; $**P < 0.001$; $***P < 0.0002$; $****P < 0.0001$; ns, not significant. We imaged half brain due to size limitations in our imaging system with the available ^{13}C coil. However, this is not an inherent limitation of eMRI, and imaging the whole brain will offer stronger signals. Brain regions not specified in Fig. 2: putamen (Put), caudate (Cau), frontal lobe (FL), parietal lobe (PL), temporal lobe (TL), occipital lobe (OL), and hypothalamus (Hyp).

multiple-comparison tests (Fig. 4*E*). To validate our ^{13}C-MRSI method and the regional variation observed, we performed phantom experiments using NMR tubes filled with ^{13}C-5mdC solutions of different concentrations. Concentration estimates by our method were in excellent agreement with the true concentrations ($r > 0.9$; *SI Appendix*, Fig. S5), confirming the accuracy of our ^{13}C-MRSI method.

Regional differences in ^{13}C-5mdC contents measured by eMRI were much stronger compared to the labeling percentage by LC-MS/MS (Fig. 4*D* versus Fig. 2*E*). This may be because eMRI measures the regional differences in total 5mdC content, thus global DNA methylation, while LC-MS measures the ratio between labeled ^{13}C-5mdC and total 5mdC. This is supported by global methylation levels measured in tissue samples from selected regions with the most significant eMRI signal differences (i.e., putamen and temporal lobe), using an enzyme-linked immunosorbent assay (ELISA). Higher global methylation was measured in putamen as compared to temporal lobe (*SI Appendix*, Fig. S6), consistent with what was observed by eMRI, supporting our hypothesis. It is possible that the labelable pool of 5mdC is similar across different brain regions, while the total 5mdC contents are variable. Finally, reducing the acquisition time by a factor of five still yielded consistent regional ^{13}C-5mdC level estimates, as compared to the original longer scan (*SI Appendix*, Fig. S7), supporting the robustness of eMRI in providing region-specific methylation measures.

Discussion

The ^{13}C-Met is incorporated in metabolic pathways that lead to the methylation of various molecules in the brain in addition to DNA—e.g., RNA and proteins—potentially generating

confounding signals in the ^{13}C-MRSI. However, the methyl and other alkyl groups on natural protein side chains have fairly large ^{13}C-NMR chemical-shift differences from the methyl group on 5mdC and should not contribute substantially to what we observe at ~13 to 15 ppm. The chemical shift for the methyl group on ^{13}C-Met residues in proteins has been shown to be mainly in the range of 17 to 19 ppm (42). The linewidth of our peak of interest was estimated to be ~1 ppm in our whole-brain ^{13}C-NMR data. Therefore, we have sufficient spectral resolution to distinguish these components, thanks to the wide chemical-shift range of ^{13}C. Even considering the potentially wider chemical-shift distributions for ^{13}C-Met in various proteins due to conformational changes and other effects, the signal from these molecules should only contribute a small broad baseline to the overall spectrum instead of the sharp peak observed in our data.

The methyl group on free Met has an expected chemical shift that is about 2 ppm different from that of 5mdC. But the labeled Met has a fast turnover rate and is thus metabolized to a negligible level within hours (43). Because we are not scanning the subject until at least several hours after the final oral dosing, the contribution of free Met to our observed signal should be very small.

While various types of methylated RNA may be present in the brain, most methyl groups on these molecules have sufficiently different chemical shifts from 5mdC in the DNA, except for methylated cytosines in the RNA (5mC). The level of messenger RNA 5mC is estimated at ~0.03 to 0.1% of cytosines, which is much rarer compared to ~4 to 5% of methylated cytosines in DNA (44). Higher methylation levels in ribosomal RNA and transfer RNA have been reported in mouse embryonic stem cells (45), but the RNA 5mC levels in mammalian brains remain largely unknown. Furthermore, the turnover rate for RNA is more rapid than for DNA (46). Therefore, we anticipate that the contribution from RNA 5mC should not significantly affect the regional variation observed by eMRI (*SI Appendix*, Fig. S7).

Another potential signal source to consider is the methyl groups on thymidine in DNA, which have a very similar chemical shift as 5mdC (~1 to 2 ppm difference; *SI Appendix*, Fig. S1). However, because thymidine is not labeled by ^{13}C-Met, the confounding background signals should predominantly come from natural-abundance ^{13}C in thymidine. Such signals are weak compared to those from labeling, especially for the 32-d-labeled samples (Fig. 3*E*). For future samples with lower labeling percentage, this background signal can be computationally removed by performing a baseline scan before labeling, followed by subtraction.

The noninvasive nature of eMRI provides a path toward a global DNA-methylation brain-imaging paradigm for humans. An important consideration for applying eMRI to humans is sensitivity. Dietary administration of ^{13}C-Met to adult humans is expected to yield a lower labeling percentage in the brain than for developing piglets (33). However, human brains have ~10× larger volume than the piglet brains imaged here, thus providing significantly larger quantities of 5mdC for signal detection. It is not difficult for humans to consume a Met-deficient diet and take ^{13}C-Met as a daily supplement. Since there is evidence supporting that the half-lives of DNA-methylation events are measured in hours (47), it likely will take less than several weeks to reach maximum labeling in humans, making this technology easily translatable. Imaging in ultrahigh-field human MRI systems (7 T or higher) should also provide a significant sensitivity boost. Furthermore, many potential optimizations in data acquisition and processing can be performed for enhancing the ^{13}C-MRSI signals.

Regional differences in brain DNA methylation have been reported for frozen samples of human brain tissue (48), but cannot be measured in intact brains due to technology limitation. eMRI bridges this gap. Our analysis of the Allen Human Brain Atlas (ABA) reveals regional differences in global gene-expression levels (*SI Appendix*, Fig. S8), which also vary with age, highlighting the importance of an in vivo approach to measure related differences. The regional gene-expression levels from the ABA do not match the regional DNA-methylation levels from the current eMRI data in any simple way, including the well-established negative relationship between gene expression and DNA promoter methylation (*SI Appendix*, Fig. S8). One possible reason is that the ABA data were from human adults, while our eMRI data are from young pigs. In addition, the canonical inverse relationship between DNA methylation and gene expression exists mainly for methylation in gene promoters, whereas eMRI measures total DNA methylation. An additional possible contributing factor to the regional eMRI signal variation is regional differences in DNA density, i.e., quantity of DNA per unit mass. While nonuniform cell densities in different mammalian brain regions have been reported (49), it is presently unclear how this nonuniformity translates to DNA density distributions. These results point to the need for more quantitative experiments on gene expression and DNA methylation to better understand the eMRI signal.

It is important to note that eMRI is able to provide information on the turnover of DNA methylation in the brain in vivo. In piglets, which have growing brains, the ^{13}C label can be incorporated into the DNA of brain cells through both new cell formation and turnover of DNA methylation, thus increasing the resulting ^{13}C labels available for MRSI detection. In adult animals and humans, however, brain growth is not a major factor, so incorporation of ^{13}C labels into the DNA of adult brain cells is primarily through turnover of DNA methylation. No previously known in vivo technique can measure this turnover, and doing so with eMRI may shed light on how the dynamics of brain DNA methylation contribute to the regulation of higher brain functions. Given the strong similarities between pig and human physiology, experimental validations on adult pigs should lay a solid foundation for human studies, which are currently being pursued (29, 50).

Although DNA methylation influences gene expression on a per-gene basis, mapping global brain DNA methylation likely provides a general measure of epignenetic activity, perhaps as a surrogate for regional gene expression, but this needs to be determined empirically. The global nature of eMRI is analogous to how fMRI measures general neuronal activity without knowledge of specific neurons. There is growing evidence suggesting the functional significance of global methylation changes, e.g., in psychiatric disorders and cancer (51, 52). eMRI may enable in vivo epigenetic study at long time scales from days to months, where such time scales are experimentally inaccessible by radioactive labeling and invasive techniques. eMRI can thus be coupled with fMRI to investigate the interaction between short-term neural and long-term molecular control of brain function, to gain further insights into the regulation of behavior and brain responses to environmental and disease stimuli.

Materials and Methods

DNA Synthesis. DNA oligonucleotides were prepared by solid-phase synthesis on an ABI 394 instrument using reagents from Glen Research, including the 5mdC phosphoramidite. Oligonucleotides were purified by 7 M urea denaturing 20% polyacrylamide gel electrophoresis with running buffer 1× TBE (89 mM each Tris and boric acid and 2 mM ethylenediaminetetraacetic acid [EDTA], pH 8.3), extracted from the polyacrylamide with TEN buffer (10 mM Tris, pH 8.0, 1 mM EDTA, and 300 mM NaCl), and precipitated with ethanol. The 20-nucleotide DNA sequence, designed to avoid self-dimer formation and to include C nucleotides in various sequence contexts, was 5′-CTACGCCTCGCTCGCCCCTT-3′, where the 10 C nucleotides were either all 5mdC or all standard dC (molecular weight 6,081 with 5mdC). Approximately 750 nmol of each oligonucleotide was dissolved in 0.5 mL

of 10% D_2O/90% H_2O (1.5 mM oligonucleotide; 9 mg/mL) in a standard 5 mm NMR tube for ^{1}H- and ^{13}C-NMR spectroscopy.

The ^{13}C-MRSI Phantom. The ^{13}C-labeled 5mdC (5-methyl cytosine-^{13}C,$^{15}N_2$ hydrochloride 99%; catalog no. M294702, Toronto Research Chemicals) was dissolved in phosphate-buffered saline (PBS) (Gibco) and then serially diluted to the desired concentrations of 1 mM, 4 mM, 6 mM, and 10 mM. The solutions were transferred to 10 mm SP Scienceware Thin Walled Precision NMR tubes (Wilmad-LabGlass), which were taped together to fit into the 30 mm probe of the 11.7 T microimaging system.

Piglet Experiments and Dietary Labeling. All animal care and experimental procedures were in accordance with the National Research Council Guide for the Care and Use of Laboratory Animals (53) and were approved by the University of Illinois Institutional Animal Care and Use Committee (Protocol 20223) (54). Naturally farrowed, intact domestic male pigs derived from the cross of Line 2 boars and Line 3 sows (Pig Improvement Company) were obtained from a commercial swine herd and transferred to the Piglet Nutrition and Cognition Laboratory (PNCL) on PND 2 ($n = 8$). Pigs were maintained at the PNCL through PND 32 per standard protocols as described elsewhere with the following modifications. All pigs were provided ad libitum access to water and a custom, nutritionally complete (55) milk-replacer formula (TestDiet) via a semiautomated liquid-delivery system that dispensed milk from 1000 to 0600 h the next day (56). The milk-replacer powder was formulated to contain 30.4% lactose, 30.3% stabilized lipids (i.e., dried fat; combination of lipid sources including sunflower oil, palm oil, and medium-chain triglycerides), and 25.4% purified amino acids; no intact protein was included in this formulation. The nutritional profile of the milk-replacer powder included 0.50% methionine and 0.49% cysteine, with the control and labeling diets containing regular L-methionine (Met) and methyl-^{13}C-L-methionine (^{13}C-Met, 99%; Sigma-Aldrich), respectively (i.e., all Met present in the labeling diet contained the stable ^{13}C isotope label). Milk-replacer formula was reconstituted fresh daily with 200 g of milk-replacer powder per 800 g of water. Pigs were individually housed in caging units (87.6 cm × 88.9 cm × 50.8 cm; length × width × height), which allowed each pig to see, hear, and smell, but not directly touch, adjacent pigs. A toy was provided to each pig for enrichment, and pigs were allowed ∼15 min of direct social interaction with other pigs once daily. The ambient environment in the rearing space was maintained on a 12 h light and dark cycle from 0800 to 2000 h, with room temperature set at 27 °C for the first 21 d of the study and gradually lowered to 22 °C during the last 7 d.

Brain Biopsy and Fixation. At the appropriate age (PND 10 and 32 d), each pig was humanely euthanized per standard protocol (57), and the whole brain was quickly excised postmortem or when meeting euthanasia criteria (58). The brain was separated into two hemispheres, with tissue samples collected from eight different regions within the left hemisphere (medial prefrontal cortex, cerebellum, hippocampus, midbrain, brainstem, thalamus, perirhinal cortex, and striatum). Enough tissue to permit the ultimate extraction of at least 1 μg of total DNA (∼100 to 250 mg) was snap-frozen on dry ice and stored at –80 °C for genomic DNA extraction. The right hemisphere from each brain remained intact (i.e., was not biopsied) and was fixed in 10% neutral-buffered formalin at 4 °C for 72 h and stored in PBS (pH 7.4; Gibco) at 4 °C for subsequent NMR spectroscopy and imaging experiments.

Genomic DNA Extraction. Pulverized tissue samples were incubated in a digestion mix (100 mM Tris, 5 mM EDTA, 200 mM NaCl, and 0.2% sodium dodecyl sulfate, pH 5.5) containing 400 $\mu g \cdot mL^{-1}$ Proteinase K (Invitrogen) and 200 $\mu g \cdot mL^{-1}$ RNase A (Invitrogen) at 50 °C overnight. Genomic DNA was extracted with phenol:chloroform:isoamyl alcohol (25:24:1 (v/v/v); Fisher Scientific) and precipitated using 70% ethanol (Sigma-Aldrich). Genomic DNA was resuspended in high-performance liquid chromatography-grade water (Sigma-Aldrich), and the concentration was measured with a NanoDrop 2000 Spectrophotometer (Thermo Fisher Scientific).

LC-MS/MS DNA Analysis. A total of 1 μg of genomic DNA was hydrolyzed overnight at 37 °C with 5 U of DNA Degradase Plus (Zymo Research) following the manufacturer's protocol in 50 μL volume. Digested DNA was filtered through Amicon Ultra 10K centrifuge filters (EMD Millipore) to remove undigested polynucleotides and collected for LC-MS/MS. LC-MS/MS analysis of ^{13}C-5mdC isotope labeling was performed with a Waters SYNAPT G2Si mass spectrometer and a Waters ACQUITY ultraperformance liquid chromatography H-class fitted with a Waters Cortecs C18+ column (2.1 × 150 mm, 1.6 μm particle size) at the flow rate of 150 $\mu L \cdot min^{-1}$ under a gradient of ammonium acetate and acetonitrile (Fisher Scientific). Multiple reaction monitoring was set up to capture the transitions from deoxycytidine to cytosine (228.1 to 112.05 Da), 5-methyldeoxycytidine to 5-methylcytosine (242.1 to 126.07 Da), and ^{13}C-5-methyldeoxycytidine to ^{13}C-5-methylcytosine (243.1 to 127.07 Da). The percentage of ^{13}C isotope labeling was determined by the following formula using peak areas of dC and 5mdC:

$$\%^{13}\text{C labeling} = 100^{*}\frac{[^{13}C\ -5mdC]}{[5mdC]+[^{13}C-5mdC]}.$$

Global DNA Methylation by ELISA. Brain tissues were collected from pigs at 32 d of age ($n = 4$; 1 female, 3 males). Putamen and temporal lobe samples (∼25 mg each) were dissected from the left hemisphere of each pig and briefly homogenized with a scalpel. Samples were then flash-frozen in liquid nitrogen and stored in cryovials at –80 °C. Genomic DNA was extracted using the DNeasy Blood & Tissue Kit (Qiagen). A Nanodrop 2000 Spectrophotometer (Thermo Fisher Scientific) was used to determine DNA concentrations. As a quality-control check, all A_{260}/A_{280} ratio values indicated sufficient DNA purity (values ranged from 1.87 to 2.02). Global DNA methylation was assessed via an ELISA-based commercial kit (MethylFlash Methylated DNA Quantification Kit [Fluorometric]; Epigentek). All standards and samples were run in duplicate. Absorbance was read at 450 nm using a plate reader (BioTek) and Gen5 (version 3.11) software. DNA-methylation levels in each brain region were calculated relative to the Methylated Control DNA standard using the single point method equation: [(Average A_{450} Sample – Average A_{450} Blank)/((Average A_{450} Methylated Control DNA – Average A_{450} Blank) × 2)] × 100%. For calculations, the quantity of each unknown sample DNA matched the quantity of Methylated Control DNA (i.e., the blanked A_{450} value for a 100 ng DNA sample was compared to the blanked A_{450} value for 100 ng of Methylated Control DNA), and the factor of 2 was to normalize the percentage of 5mC in the control DNA to 100%, as suggested in the manufacturer's instructions. This calculation yields relative global methylation level with respect to the control DNA, which is sufficient for our intended regional comparison.

Statistical Analysis. One-way ANOVA followed by Tukey's multiple-comparison test was used to compare the ^{13}C-labeling efficiencies between different brain regions, as measured by LC-MS/MS. Kruskal–Wallis followed by Dunn's multiple comparison tests were used to compare the ^{13}C-MRSI signal intensities from the different brain regions of the 32-d-labeled brain.

Brain NMR Spectroscopy and Imaging Experiments. Each intact piglet brain hemisphere was placed in a 30 mm-diameter glass tube containing perfluorocarbon oil (Fluorinert FC-40, Sigma-Aldrich) as a magnetic susceptibility matching fluid. A wooden applicator stick was taped in place to hold the brain tissue and prevent it from floating. All brain NMR spectroscopy and imaging experiments were performed using a Bruker AV3HD 11.7 T/89 mm vertical-bore microimaging system equipped with a 16-channel shim insert and Micro2.5 gradient set with a maximum gradient of 1,500 mT/m. Data were collected using a 30 mm dual-tuned ^{1}H/^{13}C radio frequency (RF) resonator and ParaVision 6.0.1 (Bruker Biospin). A 200 mM ^{13}C-Met solution dissolved in PBS was used for ^{13}C calibration before the brain-imaging scans.

MRI. During each experiment session, a localizer scan was first acquired, followed by field-map shimming. The B0 inhomogeneity was minimized to reach a ^{1}H water linewidth of between 45 and 60 Hz. Anatomical MRI scans were acquired using axial rapid acquisition with relaxation enhancement (RARE) (T2-weighted) and modified driven equilibrium Fourier transform (MDEFT) (T1-weighted) with the following parameters: RARE, repetition time (TR)/echo time (TE) = 6,000/5.5 ms, RARE factor = 4, number of averages (NA) = 2, field of view (FOV) = 30 × 30 mm^2, matrix size = 192 × 192, and 50 1-mm slices; three-dimensional (3D) MDEFT: TR/TE = 4,000/2.2 ms, inversion delay = 1,050 ms, FOV = 30(x) × 30(y) × 50(z) mm^3, matrix size = 192 × 192 × 50, and eight segments. A field map was collected covering the same FOV. Brain volume was estimated from the T1-weighted magnetic resonance (MR) image for each sample. The MR image was also segmented into 12 regions of interest (ROIs)—i.e., hippocampus, thalamus, putamen, caudate, midbrain, medial prefrontal cortex, frontal lobe, parietal lobe, temporal lobe, occipital lobe, perirhinal cortex, and hypothalamus—for regional analysis of MRSI results. The regions for tissue sampling (for LC-MS/MS and Fig. 2) were defined slightly differently from those for MRI-based segmentation, due to the difficulty in precisely extracting some regions from the piglet brains (e.g., putamen and caudate were assigned as striatum in the LC-MS/MS analysis). The cerebellum and brainstem were excluded in the imaging experiments because of the size limitation of the instrumentation used.

The ^{13}C-NMR Spectroscopy and MRSI. A whole-sample ^{13}C-NMR spectrum was collected at 125.755 MHz using a 100 μs RF pulse centered at 20 ppm, with a 2 s TR. Broadband ^{1}H decoupling was achieved with a WALTZ-16 decoupling scheme centered at 2 ppm (^{1}H carrier frequency). The free induction decay

(FID) was collected with a 22,727-Hz (~180 ppm) spectral bandwidth (BW), 1,024 points, and 16,238 averages for a total acquisition time of 9 h and 6 min. The ^{13}C-MRSI data were acquired using a phase-encoded chemical-shift imaging (CSI) sequence with a 50 μs, 30°, block RF excitation pulse; a 30 × 30 × 50 mm^3 FOV; an 8 × 8 × 8 matrix; and broadband ^{1}H decoupling described above. FIDs were collected with the same BW and number of points, TR/TE = 2,000/1.16 ms and 64 averages for a total acquisition time of 18 h and 12 min. Matching ^{1}H-CSI data were collected with TR/TE of 500/1.16 ms, 16 × 16 × 8 matrix size, and 512 FID points over a 20 ppm BW (17 min) to correct for spatial misalignment between the MRI and MRSI acquisitions.

NMR and MRSI Data Processing. A model-based data-processing method was developed to perform spectral quantification of the measured ^{13}C-MRSI data to obtain the ^{13}C-5mdC concentration maps for eMRI. The method incorporates both physics-based prior information (resonance structure of the ^{13}C-NMR spectrum) and the high signal-to-noise ratio (SNR) single-voxel spectroscopy (SVS) data from the whole sample. We first performed spectral quantification of the high-SNR SVS data, $s_{SV}(t)$, to derive spectral basis functions for our model. We expressed $s_{SV}(t)$ as:

$$s_{SV}(t) = h(t) \cdot \sum_{m=1}^{M} a_m e^{-t/T_{2,m} + i2\pi f_m t},$$

where a_m, f_m,, and $T_{2,m}$ represent concentration, resonance (chemical shift) frequency, and spin–spin relaxation constant of the m th spectral component, respectively, and $h(t)$ accounts for non-Lorentzian spectral lineshape variations introduced by nonideal experimental conditions (e.g., magnetic field drift, field inhomogeneity, etc.). In this work, $h(t)$ corresponds to a compensated Gaussian lineshape function so that the spectral model can be fit to the experimental data, with the fitting residual at the noise level and passing the Komolgrov Gaussianity test (*SI Appendix*, Fig. S3).

After spectral quantification of the SVS data, we obtained the following spectral basis functions that contain resonance frequencies and spin–spin relaxation constants of all spectral components and the spectral lineshape compensating function:

$$\varphi_m(t) = e^{-t/T_{2,m} + i2\pi f_m t} \cdot h(t), \quad m = 1, 2, \ldots, M.$$

To perform spectral quantification of the entire ^{13}C-MRSI dataset, we first mapped the data to the spatial domain using a constrained image-reconstruction method that includes B_0 field inhomogeneity correction (59). This reconstruction step included some spatial filtering effects to enhance SNR of the reconstruction. The spectral basis functions derived from the whole-sample SVS data above were used to quantify the reconstructed spatiotemporal function $\rho(x,t)$ point by point. Considering the difference in spatial resolution, shimming condition, and sequence setup between the SVS and MRSI scans, we adjusted the spectral basis functions $\varphi_m(t)$ learned from the SVS data to better match the MRSI data. To this end, we first denoised the reconstructed spatiotemporal function $\rho(x,t)$ using a low-rank filtering method (60). We then estimated a new spectral lineshape function $h(t)$ from the denoised MRSI data. The estimated lineshape function was applied to $\varphi_m(t)$ to obtain an improved set of spectral basis, $\{\hat{\varphi}_m(t)\}_{m=1}^{M}$. With $\{\hat{\varphi}_m(t)\}$ determined, concentrations, $\hat{c}_m(x)$, of all spectral components were determined from the original reconstructed spatiotemporal function $\rho(x,t)$ data by solving the following model-fitting problem (59):

$$\hat{c}_m(x) = \text{argmin} \left\| \rho(x,t) - \sum_{m=1}^{M} c_m(x)\hat{\varphi}_m(t) \right\|_2^2 + R(c_m(x)),$$

where $R(\cdot)$ represents an edge-weighting regularization function to incorporate spatial prior information. The spatial distribution of the spectral component corresponding to ^{13}C-5mdC was separated. Regional concentrations and spectra were obtained from the 12 ROIs segmented from MRI and analyzed.

Data Availability. All data are included in the manuscript and/or supporting information when possible. Custom codes were developed to analyze the ^{13}C-NMR and ^{13}C-MRSI data. The codes will be made available upon reasonable request to G.E.R. and K.C.L.

ACKNOWLEDGMENTS. We thank Dean Olson and Lingyang Zhu for discussions on ^{13}C-NMR spectroscopy and acquiring the ^{13}C-NMR data for the synthesized oligonucleotides; Furong Sun for developing the LC-MS/MS protocol and instruction on MS data analysis; Cong Zhou for his help with solid-phase DNA oligonucleotide synthesis; Yibo Zhao for his help with ^{13}C-MRSI data processing; Adam Jones for his help on piglet feeding and rearing; Joanne Fil for her help on piglet brain-tissue dissection; and Katie Ranard for her help on the DNA-methylation measurement using ELISA kits. Thanks also to the Beckman Institute for Advanced Science and Technology and the Carl R. Woese Institute for Genomic Biology for access to facilities and technical support.

1. G. E. Robinson, R. D. Fernald, D. F. Clayton, Genes and social behavior. *Science* **322**, 896–900 (2008).
2. R. Halder *et al.*, DNA methylation changes in plasticity genes accompany the formation and maintenance of memory. *Nat. Neurosci.* **19**, 102–110 (2016).
3. I. M. Traniello, G. E. Robinson, Neural and molecular mechanisms of biological embedding of social interactions. *Annu. Rev. Neurosci.* **44**, 109–128 (2021).
4. S. Ogawa, T. M. Lee, A. R. Kay, D. W. Tank, Brain magnetic resonance imaging with contrast dependent on blood oxygenation. *Proc. Natl. Acad. Sci. U.S.A.* **87**, 9868–9872 (1990).
5. J. W. Belliveau *et al.*, Functional mapping of the human visual cortex by magnetic resonance imaging. *Science* **254**, 716–719 (1991).
6. K. K. Kwong *et al.*, Dynamic magnetic resonance imaging of human brain activity during primary sensory stimulation. *Proc. Natl. Acad. Sci. U.S.A.* **89**, 5675–5679 (1992).
7. P. A. Bandettini, E. C. Wong, R. S. Hinks, R. S. Tikofsky, J. S. Hyde, Time course EPI of human brain function during task activation. *Magn. Reson. Med.* **25**, 390–397 (1992).
8. M. J. Hawrylycz *et al.*, An anatomically comprehensive atlas of the adult human brain transcriptome. *Nature* **489**, 391–399 (2012).
9. H. J. Kang *et al.*, Spatio-temporal transcriptome of the human brain. *Nature* **478**, 483–489 (2011).
10. C. L. Thompson *et al.*, A high-resolution spatiotemporal atlas of gene expression of the developing mouse brain. *Neuron* **83**, 309–323 (2014).
11. M. Gryzinska, E. Blaszczak, A. Strachecka, G. Jezewska-Witkowska, Analysis of age-related global DNA methylation in chicken. *Biochem. Genet.* **51**, 554–563 (2013).
12. G. E. Robinson, "Brains work via their genes just as much as their neurons," *The Conversation* (2015). https://theconversation.com/brains-work-via-their-genes-just-as-much-as-their-neurons-47522. Accessed 14 October 2015.
13. M. Chalfie, Y. Tu, G. Euskirchen, W. W. Ward, D. C. Prasher, Green fluorescent protein as a marker for gene expression. *Science* **263**, 802–805 (1994).
14. C. H. Contag *et al.*, Visualizing gene expression in living mammals using a bioluminescent reporter. *Photochem. Photobiol.* **66**, 523–531 (1997).
15. A. Y. Louie *et al.*, In vivo visualization of gene expression using magnetic resonance imaging. *Nat. Biotechnol.* **18**, 321–325 (2000).
16. S. W. Lee, S. H. Lee, S. Biswal, Magnetic resonance reporter gene imaging. *Theranostics* **2**, 403–412 (2012).
17. T. F. Massoud, S. S. Gambhir, Molecular imaging in living subjects: Seeing fundamental biological processes in a new light. *Genes Dev.* **17**, 545–580 (2003).
18. H. Y. Wey *et al.*, Insights into neuroepigenetics through human histone deacetylase PET imaging. *Sci. Transl. Med.* **8**, 351ra106 (2016).
19. T. M. Gilbert *et al.*, Neuroepigenetic signatures of age and sex in the living human brain. *Nat. Commun.* **10**, 2945 (2019).
20. J. J. Vaquero, P. Kinahan, Positron emission tomography: Current challenges and opportunities for technological advances in clinical and preclinical imaging systems. *Annu. Rev. Biomed. Eng.* **17**, 385–414 (2015).
21. L. Hou *et al.*, Positron emission tomography imaging of the endocannabinoid system: Opportunities and challenges in radiotracer development. *J. Med. Chem.* **64**, 123–149 (2021).
22. G. Lin, Y. L. Chung, Current opportunities and challenges of magnetic resonance spectroscopy, positron emission tomography, and mass spectrometry imaging for mapping cancer metabolism in vivo. *BioMed Res. Int.* **2014**, 625095 (2014).
23. U. Dannlowski *et al.*, Serotonin transporter gene methylation is associated with hippocampal gray matter volume. *Hum. Brain Mapp.* **35**, 5356–5367 (2014).
24. G. Ursini *et al.*, Stress-related methylation of the catechol-O-methyltransferase Val 158 allele predicts human prefrontal cognition and activity. *J. Neurosci.* **31**, 6692–6698 (2011).
25. Y. S. Nikolova *et al.*, Beyond genotype: Serotonin transporter epigenetic modification predicts human brain function. *Nat. Neurosci.* **17**, 1153–1155 (2014).
26. Y. S. Nikolova, A. R. Hariri, Can we observe epigenetic effects on human brain function? *Trends Cogn. Sci.* **19**, 366–373 (2015).
27. J. Richiardi *et al.*, Correlated gene expression supports synchronous activity in brain networks. *Science* **348**, 1241–1244 (2015).
28. M. H. Puglia, T. S. Lillard, J. P. Morris, J. J. Connelly, Epigenetic modification of the oxytocin receptor gene influences the perception of anger and fear in the human brain. *Proc. Natl. Acad. Sci. U.S.A.* **112**, 3308–3313 (2015).
29. B. Hoffe, M. R. Holahan, The use of pigs as a translational model for studying neurodegenerative diseases. *Front. Physiol.* **10**, 838 (2019).
30. L. A. O'Tuama *et al.*, L-methionine uptake by human cerebral cortex: Maturation from infancy to old age. *J. Nucl. Med.* **32**, 16–22 (1991).
31. C. Valdovinos-Flores, M. E. Gonsebatt, The role of amino acid transporters in GSH synthesis in the blood-brain barrier and central nervous system. *Neurochem. Int.* **61**, 405–414 (2012).
32. R. Zaragozá, Transport of amino acids across the blood-brain barrier. *Front. Physiol.* **11**, 973 (2020).

33. M. Bachman *et al.*, 5-Hydroxymethylcytosine is a predominantly stable DNA modification. *Nat. Chem.* **6**, 1049–1055 (2014).
34. R. Wilhelm, A. Szeitz, T. L. Klassen, W. W. Mohn, Sensitive, efficient quantitation of ^{13}C-enriched nucleic acids via ultrahigh-performance liquid chromatography-tandem mass spectrometry for applications in stable isotope probing. *Appl. Environ. Microbiol.* **80**, 7206–7211 (2014).
35. P. Tognini *et al.*, Experience-dependent DNA methylation regulates plasticity in the developing visual cortex. *Nat. Neurosci.* **18**, 956–958 (2015).
36. A. M. M. Oliveira, DNA methylation: A permissive mark in memory formation and maintenance. *Learn. Mem.* **23**, 587–593 (2016).
37. E. N. W. Wheater *et al.*, DNA methylation and brain structure and function across the life course: A systematic review. *Neurosci. Biobehav. Rev.* **113**, 133–156 (2020).
38. S. Li, J. Yang, J. Shen, Novel strategy for cerebral ^{13}C MRS using very low RF power for proton decoupling. *Magn. Reson. Med.* **57**, 265–271 (2007).
39. C. I. H. C. Nabuurs, D. W. J. Klomp, A. Veltien, H. E. Kan, A. Heerschap, Localized sensitivity enhanced in vivo ^{13}C MRS to detect glucose metabolism in the mouse brain. *Magn. Reson. Med.* **59**, 626–630 (2008).
40. J. N. Hyacinthe *et al.*, Evaluating the potential of hyperpolarised [1-^{13}C] L-lactate as a neuroprotectant metabolic biosensor for stroke. *Sci. Rep.* **10**, 5507 (2020).
41. V. Ruiz-Rodado, J. R. Brender, M. K. Cherukuri, M. R. Gilbert, M. Larion, Magnetic resonance spectroscopy for the study of CNS malignancies. *Prog. Nucl. Magn. Reson. Spectrosc.* **122**, 23–41 (2021).
42. G. L. Butterfoss *et al.*, Conformational dependence of ^{13}C shielding and coupling constants for methionine methyl groups. *J. Biomol. NMR* **48**, 31–47 (2010).
43. L. Milazzo *et al.*, [^{13}C]Methionine breath test: A novel method to detect antiretroviral drug-related mitochondrial toxicity. *J. Antimicrob. Chemother.* **55**, 84–89 (2005).
44. D. Wiener, S. Schwartz, The epitranscriptome beyond m^{6}A. *Nat. Rev. Genet.* **22**, 119–131 (2021).
45. C. Legrand *et al.*, Statistically robust methylation calling for whole-transcriptome bisulfite sequencing reveals distinct methylation patterns for mouse RNAs. *Genome Res.* **27**, 1589–1596 (2017).
46. J. Defoiche *et al.*, Measurement of ribosomal RNA turnover in vivo by use of deuterium-labeled glucose. *Clin. Chem.* **55**, 1824–1833 (2009).
47. R. B. Meagher, 'Memory and molecular turnover,' 30 years after inception. *Epigenetics Chromatin* **7**, 37 (2014).
48. C. Ladd-Acosta *et al.*, DNA methylation signatures within the human brain. *Am. J. Hum. Genet.* **81**, 1304–1315 (2007).
49. S. Herculano-Houzel, C. E. Collins, P. Wong, J. H. Kaas, R. Lent, The basic nonuniformity of the cerebral cortex. *Proc. Natl. Acad. Sci. U.S.A.* **105**, 12593–12598 (2008).
50. D. K. C. Cooper, B. Ekser, A. J. Tector, A brief history of clinical xenotransplantation. *Int. J. Surg.* **23** (Pt B), 205–210 (2015).
51. Q. Du *et al.*, DNA methylation is required to maintain both DNA replication timing precision and 3D genome organization integrity. *Cell Rep.* **36**, 109722 (2021).
52. C. Liu, C. Jiao, K. Wang, N. Yuan, DNA methylation and psychiatric disorders. *Prog. Mol. Biol. Transl. Sci.* **157**, 175–232 (2018).
53. National Research Council, *Guide for the Care and Use of Laboratory Animals* (National Academies Press, Washington, DC, ed. 8, 2011).
54. Federation of Animal Science Societies, *Guide for the care and use of agricultural animals in research and teaching, 4th ed.* (Champaign, IL, 2020).
55. National Research Council, *Nutrient Requirements of Swine: Eleventh revised edition.* The National Academies Press, Washington, DC (2012).
56. J. E. Fil, S. Joung, C. A. Hayes, R. N. Dilger, Influence of rearing environment on longitudinal brain development, object recognition memory, and exploratory behaviors in the domestic pig (*Sus scrofa*). *Front. Neurosci.* **15**, 649536 (2021).
57. S. Leary *et al.*, *AVMA Guidelines for the Euthanasia of Animals: 2020 Edition* (American Veterinary Medical Association, Schaumburg, IL, 2020).
58. S. A. Fleming, S. Monaikul, A. T. Mudd, R. Jacob, R. N. Dilger, Extraction and dissection of the domesticated pig brain. *J. Vis. Exp.* **2021**, e62030 (2021).
59. F. Lam, Z.-P. Liang, A subspace approach to high-resolution spectroscopic imaging. *Magn. Reson. Med.* **71**, 1349–1357 (2014).
60. H. M. Nguyen, X. Peng, M. N. Do, Z. P. Liang, Denoising MR spectroscopic imaging data with low-rank approximations. *IEEE Trans. Biomed. Eng.* **60**, 78–89 (2013).